ADVANCED MATERIALS TECHNOLOGIES
www.advmattechnol.de

A Scalable Fully Printed Organic Thermoelectric Generator for Harsh Environments Enabled by a Stable n-type Polymer

*Irene Brunetti, Nathan James Pataki, Diego R. Hinojosa, Angus Hawkey, Ozan Karakaya, Christian Rainer, Muhammad Irfan Khan, Leonard Franke, Md Mofasser Mallick, Gerardo Hernandez-Sosa, Martijn Kemerink, Mario Caironi, and Uli Lemmer**

Affordable and versatile power sources become crucial as miniaturized electronics and sensors become more widespread. Organic thermoelectric generators (TEGs), capable of tapping into wasted heat sustainably and economically, are viewed as key enablers for powering the sensor networks of the future. Until recently, the performance of n-type organic thermoelectric materials has severely lagged behind their p-type counterparts. However, reports of a stable and highly conductive n-type polymer, poly(benzodifurandione) (PBFDO), are changing this notion. Nonetheless, validation of PBFDO as a suitable ink for scalable fabrication processes and integration of the material into a scalable organic TEG have yet to be demonstrated. This work presents the development, characterization, and optimization of a PBFDO ink for use in a scalable inkjet printing process. The n-type ink is then integrated into a screen-printed origami-inspired architecture, resulting in a 21-leg PEDOT:PSS/PBFDO organic TEG capable of delivering a record-high normalized power density among reported polymer-based TEGs of 0.718 nW cm^{-2} K^{-2}. Moreover, the module ambient stability is demonstrated for up to 90 d, while its use for potential applications in harsh environments is validated for a temperature range of -8 °C to 200 °C and up to 90% relative humidity, a first for organic TEGs.

1. Introduction

As distributed microelectronics and sensors proliferate, it is evident that versatile and sustainable decentralized power sources will need to accompany such applications. Thermoelectric generators (TEGs) are sustainable heat-harvesting devices that convert low-grade thermal energy (<200 °C) into electric power by way of the Seebeck effect.[1] TEGs constitute an important part of the future energy landscape since they do not need to be recharged, can operate in the absence of light, and do not require any moving elements, thus complementing the shortcomings of batteries, photovoltaics, piezoelectrics, and triboelectrics. In particular, organic TEGs made from small molecules or polymeric materials can be flexible and lightweight, and are compatible with scalable printing techniques, making them ideal candidates for small-scale power generation

I. Brunetti, O. Karakaya, C. Rainer, M. I. Khan, L. Franke, M. M. Mallick, G. Hernandez-Sosa, U. Lemmer
Light Technology Institute (LTI)
Karlsruhe Institute of Technology (KIT)
Engesserstr. 13, 76131 Karlsruhe, Germany
E-mail: uli.lemmer@kit.edu

I. Brunetti, O. Karakaya, C. Rainer, G. Hernandez-Sosa, U. Lemmer
InnovationLab GmbH
Speyerer Strasse 4, 69115 Heidelberg, Germany

N. James Pataki, M. Caironi
Center for Nano Science
Technology
Istituto Italiano di Tecnologia
Via Raffaele Rubattino, 81, Milan 20134, Italy

The ORCID identification number(s) for the author(s) of this article can be found under https://doi.org/10.1002/admt.202400968

DOI: 10.1002/admt.202400968

N. James Pataki
Department of Physics
Politecnico di Milano
Piazza Leonardo da Vinci 32, Milano 20133, Italy

D. R. Hinojosa
Technische Universität Chemnitz
Institut für Chemie
Straße der Nationen 62, 09111 Chemnitz, Germany

A. Hawkey
Institute for Physical Chemistry
Heidelberg University
Im Neuenheimer Feld 253, 69120 Heidelberg, Germany

G. Hernandez-Sosa, U. Lemmer
Institute for Microstructure Technology (IMT)
Karlsruhe Institute of Technology (KIT)
Hermann-von-Helmholtz Platz 1, 76344 Eggenstein-Leopoldshafen, Germany

M. Kemerink
Institute for Molecular Systems Engineering and Advanced Materials
Heidelberg University
Im Neuenheimer Feld 225, 69120 Heidelberg, Germany

in Internet of Things devices.[2] These attributes of organic thermoelectric materials, along with the absence of rare elements and energy-intensive processing methods, are especially beneficial for powering wearables,[3] agricultural and industrial sensors,[4] and point-of-care devices[5,6] where high conformability, a modest price-point, and a compact form-factor are highly valued.

Examples of printed organic TEGs that exploit the production potential of high-throughput large-area techniques such as screen-printing, roll-to-roll printing, and inkjet printing can be found in literature,[7–9] but they fall well short of the power demands for even the most efficient low-power microelectronics, which need several tens to hundreds of μW.[4,10,11] One significant reason for the laggard progress has been the lack of highly conductive and air-stable n-type organic thermoelectric materials, which typically degrade in a matter of minutes when exposed to air after being doped, and only exhibit electrical conductivities in the range of σ = 0.1–100 S cm^{-1}.[11–15] When compared to p-type materials where σ > 1000 S cm^{-1} and ambient stability are frequently reported,[16–18] n-type materials lag significantly behind, although they are catching up in terms of performance and stability.[19,20] The reasons for this are multifactorial, but poor doping efficiency and unstable radical anions as a result of insufficiently deep energy levels of the lowest unoccupied molecular orbitals (LUMOs) are among the principal causes.[21]

In order to maximize the conversion efficiency of organic TEGs and move toward power outputs that might have a real-world impact, both high-performing p-type and n-type materials are necessary. The maximum power density of any TEG under load-matching conditions, where the load resistance equals the internal resistance of the TEG, $R_{load} = R_{TEG}$, can be written as:

$$P_{density} = \frac{n^2\left(S_p - S_n\right)^2}{4R_{TEG}A_{TEG}}\Delta T^2 \quad (1)$$

where n is the number of thermocouples, S_p and S_n are the Seebeck coefficients of the p-type and n-type thermoelements respectively, A_{TEG} is the cross-sectional area of the TEG perpendicular to the direction of heat flux, and ΔT is the temperature difference across the thermoelements. In the absence of stable n-type materials, reports of organic TEGs in literature often present unipolar devices where the n-type leg is shorted with a conductive, but almost thermoelectrically inactive, trace.[22] Conversely, reports that present fully organic TEGs with active n-type and p-type thermoelements, often make no mention of the ambient stability of the device.[8,23,24]

The significant gap between the performance of n-type and p-type organic thermoelectric materials was bridged in 2022 when researchers reported the facile synthesis of a highly conductive n-type polymer, poly(benzodifurandione) (PBFDO).[25,26] The reports described an n-type polymer that exhibited excellent ambient stability, electrical conductivities σ > 2000 S cm^{-1}, and a synthetic simplicity that it might offer a potential for a revolution in the field of organic thermoelectrics. Since the initial publications, a PBFDO coated silk yarn has been incorporated into a TEG,[27] but there have not been any demonstrations of fully printed TEGs that incorporate PBFDO into scalable architectures. Organic TEGs found in literature often present devices with <10 thermocouples and extrapolate the performance of larger devices without demonstrating scalability.[8,28] Doing so, the challenges of scaling up are largely ignored.[29]

The initial reports of PBFDO implied that the n-type polymer would represent a paradigm shift in organic thermoelectrics due to its stability and conductivity, yet questions about its adaptability to printing techniques have been unanswered and demonstrations of scalable application-focused devices have not been reported. Here, those questions are considered by demonstrating the printability of a DMSO-based PBFDO ink with a solution-based deposition technique and by integrating the n-type polymer into a scalable 21-legs organic TEG. The fabrication process exploits inkjet and screen-printing methods to pattern an origami-inspired architecture onto an ultrathin and flexible parylene substrate that maximizes power density, reaching a maximum power density of 2.69 μW cm^{-2} at ΔT = 61 K. The ambient stability of the device is demonstrated over a period of eight weeks. In addition, an excellent stability in harsh environments ranging from −8 °C to 200 °C and 0% to 90% relative humidity is reported.

Compared to other reported devices, the organic TEG presented in this work represents the highest reported normalized power output of 0.718 nW cm^{-2} K^{-2} among other reported organic TEGs. Significantly, this is the first study to validate the long-term operational stability of an organic TEG over a wide range of temperatures and humidity levels. The printability of the PBFDO ink, the scalable origami architecture, and the demonstrated operational stability collectively represent a major advancement for organic TEGs and their potential for real-world applications.

2. Results

2.1. Development of the PBFDO Ink

PBFDO in DMSO was synthesized by the previously reported quinone radical homocoupling reaction resulting in oxidative polymerization and reductive doping of the electron-deficient 3,7-dihydrobenzo[1,2-*b*:4,5-*b*′]difuran-2,6-dione (H-BFDO) monomer (**Figure 1a**).[25] PBFDO ink was synthesized in tens of milliliters quantities using tetramethylquinone (TMQ) as radical initiator and remained stable in solution under ambient conditions for weeks (Figures 1b and S1, Supporting Information). The final concentration of the solution was adjusted to 10 mg mL^{-1} with respect to the 3,7-dihydrobenzo[1,2-*b*:4,5-*b*′]difuran-2,6-dione (BDF) monomer from the crude reaction mixture and directly purified in a dialysis sack with an average molecular weight (M_n) cutoff of 10 kDa.

To pattern PBFDO with an inkjet printer, an ink was developed such that it would have the surface tension and viscosity to form homogenous and stable droplets. The printability of an ink depends on a number of factors, including the surface tension γ, density ρ, and dynamic viscosity η. These properties, along with the printing parameters such as nozzle size d, and fluid drop velocity v, can be expressed as the Reynolds number Re, and the Weber number We.

$$\mathrm{Re} = \frac{\rho v d}{\eta} \quad (2)$$

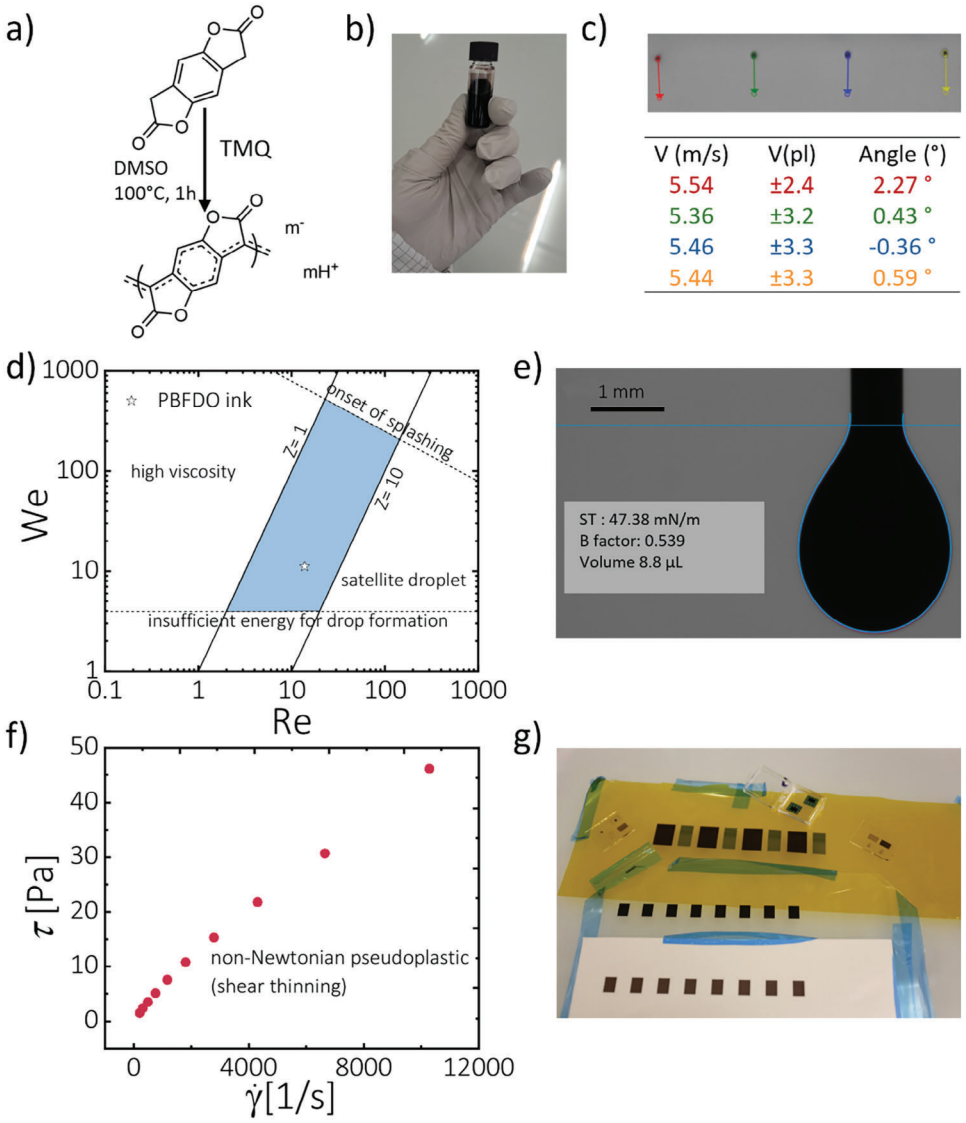

Figure 1. a) Reaction scheme of PBFDO. b) Milliliter-scale facile synthesis of the PBDFO ink. c) Fluid drop velocity using the PixDro LP50. The velocity expressed in m s^{-1}, volume in pL, and angle in ° are reported in the table. The colors of the rows correspond to the characteristics of the drops with the arrow of the same color. d) Weber number plotted versus the Reynolds number with the area of the inverse Ohnesorge number between $1 < Z < 10$ shown in blue. The PBFDO ink is located within the printability zone (white star). e) Surface tension (ST) of the formed droplet of the PBFDO ink. f) Measurement of ink viscosity: shear stress (τ) as a function of the shear rate ($\dot{\gamma}$). g) Photograph of PBFDO film on different substrates: polyimide, parylene, ethyl-cellulose, glass, and silicon.

$$\mathrm{We} = \frac{\rho v^2 d}{\gamma} \tag{3}$$

These dimensionless parameters are commonly rolled into a single figure of merit known as the inverse Ohnesorge number Z, which ideally falls between a value of $Z = 1$ and $Z = 10$.

$$Z = \mathrm{Oh}^{-1} = \frac{\mathrm{Re}}{\sqrt{\mathrm{We}}} = \frac{\sqrt{\rho\gamma d}}{\eta} \tag{4}$$

The ink was optimized to a concentration of 10 mg mL^{-1}, such that the ink fluid drop velocity was 5.4 m s^{-1} (Figure 1c), the viscosity was 7.5 mPa s (Figure 1f), the surface tension (ST) was 47.38 mN m^{-1} (Figure 1e), and the density of the ink was 1.1 g cm^{-3}. The Reynolds number and Weber number of the ink are plotted in Figure 1d, showing that the optimized ink has an inverse Ohnesorge number of $Z = 4.14$, which falls within the targeted zone for sufficient energy for drop formation, without the emergence of satellite droplet formation and the onset of splashing. The printability of the PBFDO ink on polyimide, parylene, ethyl-cellulose, glass, and silicon substrates was validated using a PixDro LP50 printer (Figures 1g and S2, Supporting Information).

The sheet resistance R_S and in-plane electrical conductivity σ of the printed PBFDO were measured as a function of an

increasing number of printed layers. The inverse relationship between R_S and thickness, and the constant trendline between σ and thickness demonstrate a well-behaved system whose properties do not change with additional printed layers (**Figure** 2a), an important aspect for scalable fabrication. The electrical conductivity, Seebeck coefficient, and in-plane thermal conductivity of the printed PBFDO film (4 µm thick) were characterized with respect to temperature using a Linseis TFA thermoelectric characterization system. The room temperature electrical conductivity and the Seebeck coefficient of the inkjet printed films were found to be $\sigma = 175$ S cm^{-1} and $S = -20$ µV K^{-1} (Figure 2b). The $\sigma = 175$ S cm^{-1} of the inkjet-printed PBFDO films is lower than the values reported for spin-coated films, while the measured Seebeck coefficients of both are well-aligned.[25] The discrepancy in the measured σ is likely due to the variations caused by differing deposition methods. For instance, a recent study on PBFDO-coated silk yarn for thermoelectric applications reported an electrical conductivity of just $\sigma = 13$ S cm^{-1} and attributes the difference in conductivity to variations in nanostructure as a result of processing techniques, i.e., drop casting compared to spin coating.[27] Another potential factor for the subdued σ could be the formation of structural defects along the polymer backbone, such as the isomerization from isoxindigo to dibenzonaphthyrone if the synthetic conditions are not strictly controlled.[26,30] In other words, some undesired units can be incorporated into the PBFDO backbone during the polymerization and impinge on the performance of the material.

Examining the temperature dependence of electrical conductivity, the increase in σ as a function of increasing temperature indicates that σ is weakly activated with increasing temperature, as is expected for disordered semiconductors.[31] The ln(σ) as a function of inverse temperature exhibited a decreasing but nonlinear trend; consequently, it was not feasible to assess a well-defined activation energy (Figure S3, Supporting Information). The positive trend observed in the log-log plot of the reduced activation energy $W = [\mathrm{d}(\ln\sigma)/\mathrm{d}(\ln T)]$ as a function of the temperature (Figure S4, Supporting Information) suggests an approach to metal-like behavior. Tang et al. similarly conclude that the charge-transport mechanism in the highly doped conducting polymer PBFDO is located in the critical region of the metal-insulator transition, characterized by record-high room-temperature Hall mobilities of 1.01 cm^2 V^{-1} s^{-1}.[25] It has been suggested that the high mobility of PBFDO is in part due to the side-chain-free structure and high backbone planarity.[26]

The in-plane thermal conductivity of the PBFDO thin film was not characterized in previous reports, but here was found to be equal to $\kappa = 2.2$ W m^{-1} K^{-1} at room temperature (Figure 2c). The relatively high thermal conductivity for this organic material can be tentatively attributed to the absence of soft, solubilizing side chains that are characteristic of virtually all other organic thermoelectric polymers.[19] In the absence of these side chains, phonon-like waves can travel longer distances without being scattered, resulting in a higher thermal lattice contribution, which, in this case, is the major contributor to the overall thermal conductivity (Figure S5, Supporting Information). The dimensionless figure of merit, $zT = \sigma S^2 T/\kappa$ is also plotted for the printed PBFDO films in Figure 2c.

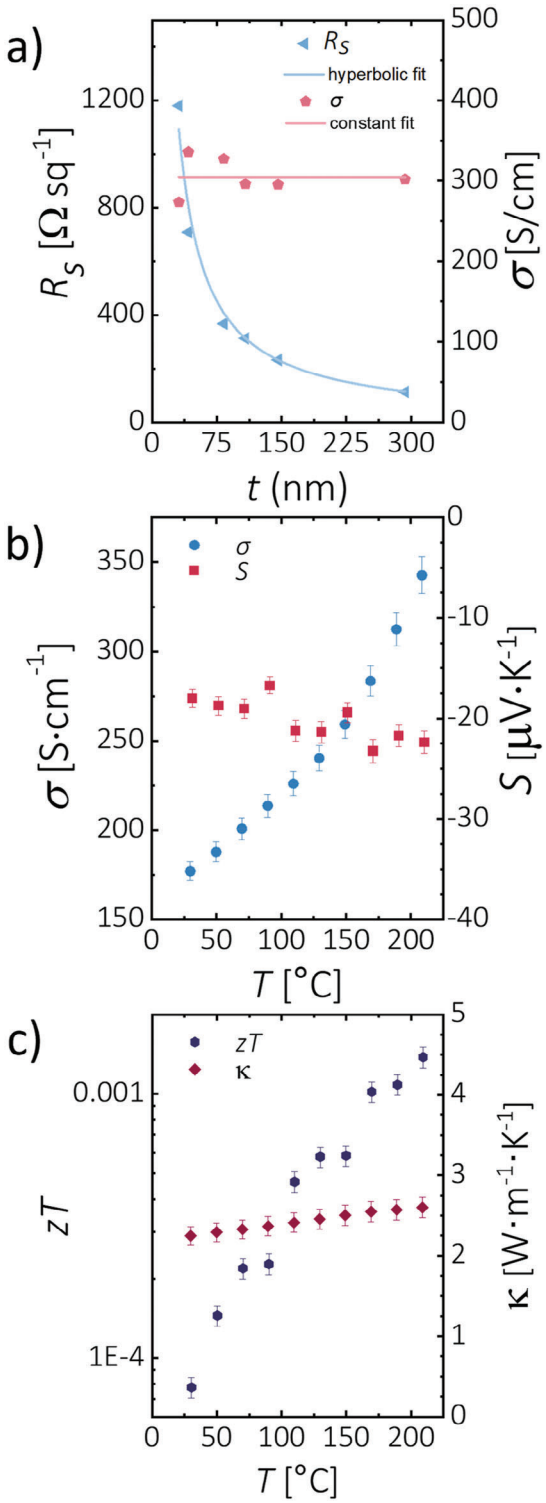

Figure 2. a) Electrical conductivity (red pentagons) with a constant fitting (red line) and sheet resistance (blue triangles) with a hyperbolic fitting of a printed PBFDO film with respect to the thickness of the printed film. b) Electrical conductivity (blue circles) and Seebeck coefficient (red squares) of an inkjet printed PBFDO film as a function of measurement temperature. c) Figure of merit, zT (blue hexagons), and thermal conductivity (red diamonds) of the inkjet printed PBFDO film as a function of measurement temperature.

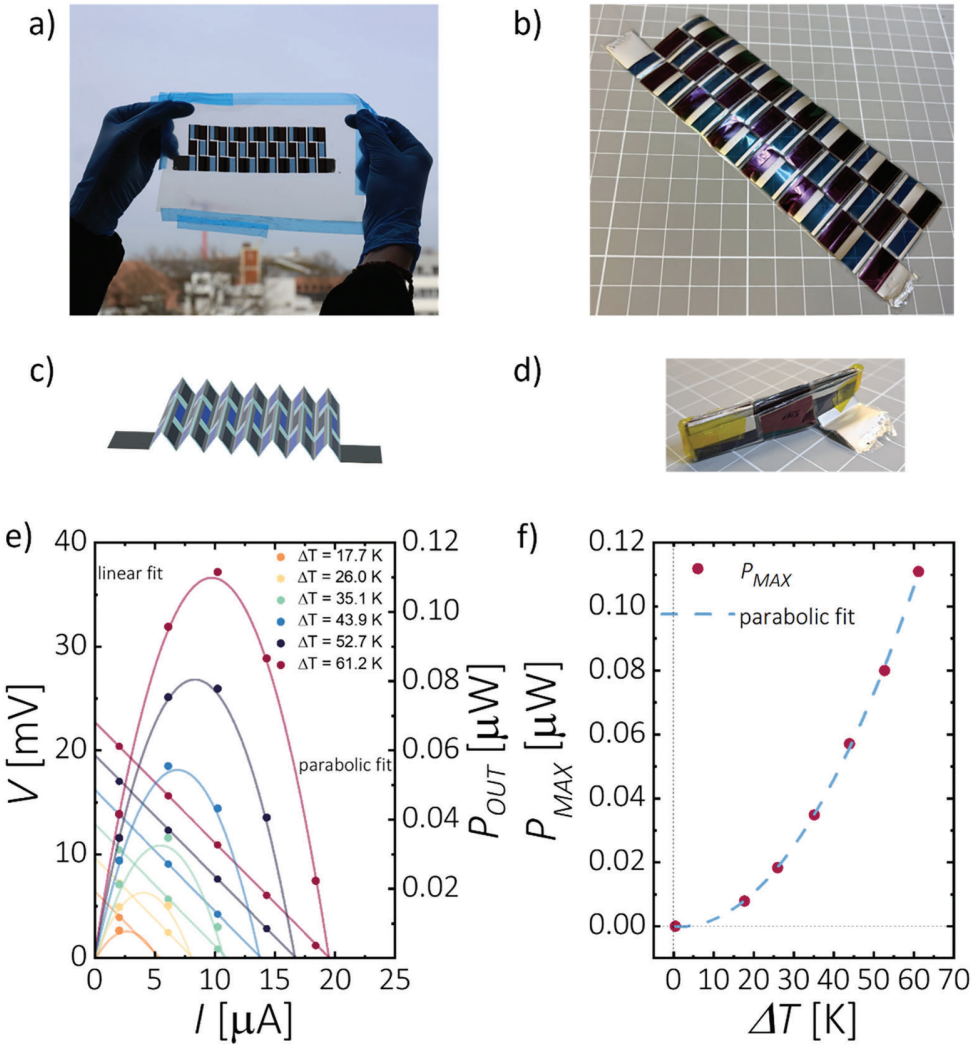

Figure 3. a) Image of the PEDOT:PSS (blue legs)/PBFDO (black legs) TEG after printing on a thin parylene C layer while on a PEN carrier. b) Image of the PEDOT:PSS/PBFDO TEG after delamination from the PEN carrier. c) Scheme of the folding process. d) Image of the folded PEDOT:PSS/PBFDO TEG. e) Voltage (incl. linear fit) and power output (incl parabolic fit) plotted against the current for the PEDOT:PSS/PBFDO TEG characterized at $\Delta T =$ 17.7 K to $\Delta T =$ 61.2 K. f) Maximum power density (incl. a parabolic fit) of the folded TEG as a function of the temperature gradient.

2.2. Fabrication and Characterization of the Scalable Folded TEG

For the fabrication of the scalable folded TEG, a commercial poly(3,4-ethylenedioxythiophene) polystyrene sulfonate (PEDOT:PSS) ink formulated for screen-printing (Clevious SV4 PEDOT:PSS) was used for the p-type thermoelements. A silver nanoparticle (AgNP) ink (LOCTITE ECI 1010 E&C) was used to pattern the conductive electrodes. The used origami TEG is an advantageous design that exploits scalable planar deposition techniques such as screen-printing and inkjet printing to pattern a 2D architecture, yet the final folded 3D conformation improves the thermal impedance matching with the heat source and heat sink.[32] In this work, parylene C was deposited by chemical vapor deposition on a PEN carrier and was used as the flexible substrate upon which the architecture is patterned. Parylene C is ideal since the thickness, and therefore the cross-sectional area of the folded device could be minimized to maximize the power density of the organic TEG. A 3.8 μm layer was used as the base substrate, and a 0.7 μm encapsulating layer was deposited after printing but before folding to electrically insulate the thermoelements once the device was folded.

The folded architecture used for this work consisted of 21 thermocouples (14 folded stripes), with each thermoelement measuring 8.5 mm wide and 14.8 mm long (**Figure 3a**). This architecture is an improved iteration of a previously reported design,[32,33] and with the main benefits being fewer folds, and refraining from utilizing additional time and resource-consuming cutting steps. The folded edges are regions of high mechanical strain, which can result in irreversible damage to the device if cracking or splitting occurs. Eight layers of the PEDOT:PSS ink and two layers of the AgNP ink were screen-printed with a fine 125-35y/22° SAATILENE Hitex screen onto the parylene substrate. After annealing, the *n*-type thermoelements were patterned with the DMSO-based PBFDO ink (10 mg mL^{-1}) and

Table 1. Polymer-based organic TEGs reported in literature and some of the relevant variables such as number of thermocouples (n), device area (A_{TEG}), temperature gradient used for maximum power measurement (ΔT), maximum power output (P_{out}), maximum power density ($P_{density}$), normalized power density, normalized power output (Φ_p), viable storage temperature range (T), and shelf-life duration (t).

References	p-type material	n-type material	Fabrication method [s]	n	A_{TEG} [cm^{-2}]	ΔT [K]	P_{out} [W]	$P_{density}$ [$\mu W\ cm^{-2}$]	Φ_p [$pW\ cm^{-2}\ K^{-2}$]	T	t [days]
[37]	PEDOT:PSS	–	Screen printing	162	196	85.5	3.20×10^{-7}	0.002	0.22	–	–
[38]	PEDOT:Tos	–	Dispenser printing	30	9	80	0.4×10^{-7}	0.004	0.69	–	–
[39]	PEDOT:PSS	–	Submersion-coating of fibers	8	28.1	65	1.22×10^{-6}	0.04	10.28	–	–
[40]	PEDOT:PSS	–	Thermal evaporation/ spray-coating	24	7.2	17.5	1.00×10^{-6}	0.14	453.5	–	–
[41]	PEDOT:PSS	FBDPPV:TAM	Thermal evaporation/ photolithography/drop-casting	3	13.2	46.5	7.70×10^{-8}	0.01	2.70	–	–
[14]	TBDOPV-T-518:$FeCl_3$	TBDOPV-T-518:DMBI	Thermal evaporation/ drop-casting	3	21.6	45.1	4.03×10^{-7}	0.02	9.17	–	–
[24]	PEDOT:PSS	PBFDO	Drop-casting	6	29.7	135	1.95×10^{-6}	0.07	3.60	–	–
[24]	PEDOT:PSS	PTEG-1	Laser ablation/ inkjet printing	48	1	25.0	3.05×10^{-8}	0.03	48.80	–	–
[8]	PEDOT:PSS	BBL:PEI	Inkjet printing/ spray-coating	4	0.001	50.0	3.30×10^{-10}	0.15	60.83	–	–
This work	PEDOT:PSS	PBFDO	Screen printing/ inkjet printing	21	0.041	61.2	1.1×10^{-7}	2.69	718	−8 to 200 °C	>90

PixDro LP50 inkjet printer (20 layers). The layouts of the screens are reported in Figures S6 and S7 (Supporting Information). The internal resistance of the 21-leg TEG was found to be R_{TEG} = 1180 Ω. The thickness of the printed layers was measured using a Dektak profilometer, the maximum total thickness of the printed devices was 1.7 µm corresponding to the stack of PEDOT:PSS and the silver contact, not considering the substrate.

After encapsulation (Figures 3b and S8 Supporting Information) and folding (Figure 3c,d), the performance of the organic TEG was characterized using a custom-built TEG measurement setup in which the temperature of a copper heat source and heat sink can be varied between 273 K and 363 K. The folded TEG is vertically sandwiched between the heat source and heat sink. Thermally conductive paste (FEROTHERM 4) was applied at the contact points between the TEG and the Copper blocks to enhance thermal coupling. The current–voltage (I–V) characteristics of the TEG were characterized using a maximum power point tracking method with a source measurement unit (SMU) after a stable temperature difference ΔT was established between the Copper blocks. The organic TEG was characterized under temperature differences ranging from ΔT = 17.7 K to ΔT = 61.2 K, resulting in a maximum power output of P_{max} = 0.11 µW and an open-circuit voltage of V_{OC} = 22.48 mV at a ΔT = 61.2 K (Figure 3d), while an ideal linear dependence of V with respect to I and a parabolic relationship between P_{out} and I are observed. The TEG characterization was conducted with a T_c around 20 °C and a T_h values ranging from 20 °C to 80 °C for a prolonged period of time (over 1 h). These findings highlight how the TEG operates correctly even at high $T_m = (T_h + T_c)/2$ for an extended period, thanks to relatively stable zTs of the organic printed materials. Each curve in Figure 3e is the result of the average of 5 cycles repeated every 35 s after reaching a stable ΔT. The cycles of the $T_m = (T_h + T_c)/2 = (19.9 + 72.6)/2$ °C = 46.3 °C are reported in Figure S9 (Supporting Information).

TEGs reported in literature vary widely in their size, shape, and characterization conditions. Normalized metrics like power density, $P_{density} = P_{out}/A_{TEG}$, and TEG power factor, $\phi_P = P_{out}/(A_{TEG}\ T^2)$ facilitate comparisons across devices. The power density for this folded TEG was calculated using the cross-sectional area of the module measured using a µm-screw gauge ($A_{TEG} = 4.9 \times 10^{-6}\ m^2$) and aligned well with the theoretical cross-sectional area ($A_{TEG} = 4.08 \times 10^{-6}\ m^2$) considering the thicknesses of the printed layers and the width of the legs. The maximum power density was measured to be $P_{density}$ = 2.69 µW cm^{-2} at ΔT = 61.2 K, and the TEG power factor was calculated to be ϕ_P = 0.718 nW cm^{-2} K^{-2}. As shown in **Table 1**, this value is significantly higher than the values reported for other organic TEGs.

Finite element analysis simulations of a device with three thermoelements (two folded stripes) were conducted to assess whether the experimental performance of the PEDOT:PSS/PBFDO module (thermoelectric properties used are reported in Table S1, Supporting information) matches the nominal values expected on basis of the material properties. **Figure** 4a shows the simulated power output of the module multiplied by a factor of seven compared to the measured experimental power output (14 folded stripes), while Figure 4b depicts the temperature distribution across the geometry of the simulated device. The simulated and experimental values for the maximum power outputs are in good agreement and are only differing by 9.75% with a ΔT = 61.2 K. This small discrepancy can be attributed to slight variations in the thickness of the printed films, a complex measurement within thin films on flexible substrate, leading to differences in the internal resistances of the experimental and simulated devices. However, as the simulations overestimate the resistance, the maximum power point is shifted to lower current values. The agreement between simulated and experimental results further attests to the scalability of the materials and reproducibility of the architecture. An architecture or fabrication method that lacks reproducibility and scalability would result in experimental devices deviating further from ideal performance as the number of thermocouples (n) increases.

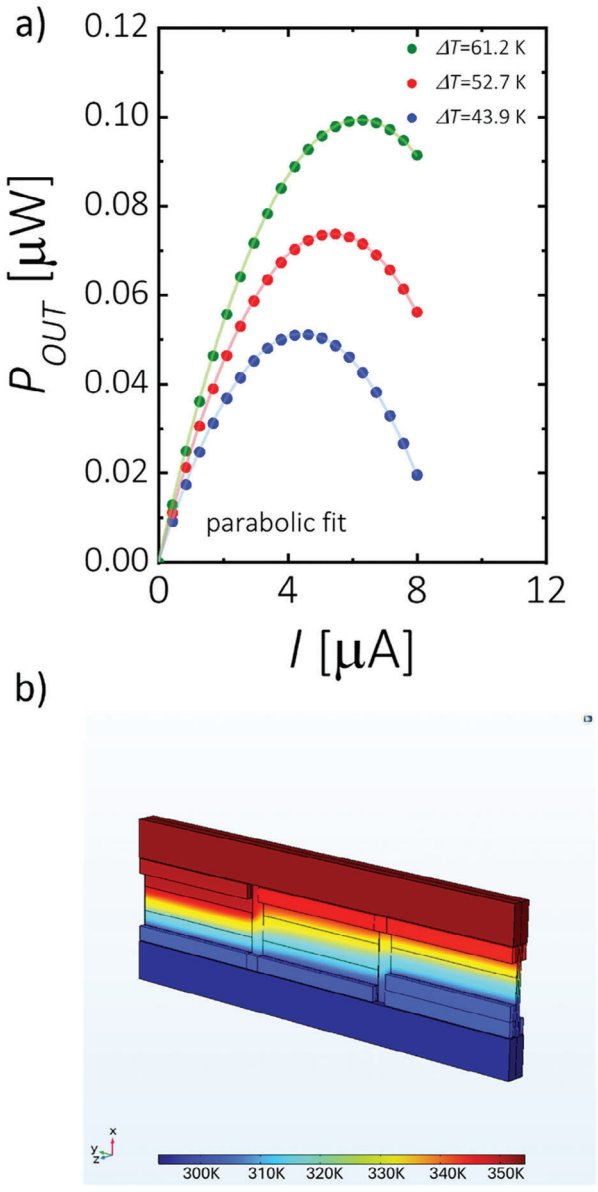

Figure 4. a) Simulated power output of the PEDOT:PSS/PBFDO module generated using finite element analysis. b) Temperature distribution across the geometry of the simulated PEDOT:PSS/PBFDO module with an applied temperature gradient of $\Delta T = 61.2$ K. Note that the z-axis is magnified by a factor 50.

2.3. Stability in Harsh Environments

Validating the stability of organic TEGs in environments that mimic potential use case scenarios is crucial for any application-focused device. However, the often underwhelming stability of p-type and particularly n-type organic thermoelectric materials, while slowly improving,[34–36] has led to shelf-life being rarely tested and reported. The PEDOT:PSS/PBFDO TEG reported here showed ambient shelf-life stability at room temperature for over 3 months with less than 5% change in the internal resistance (**Figure** 5a). To test stability in hostile environments, a TEG with six thermoelements was printed on a Kapton substrate with a thickness of 25 µm (Figure S10, Supporting information), following the procedure described in the previous section. The second module exploited a Kapton substrate for easier handling, demonstrating the versatility of the fabrication process with different substrates; however, the thin layer of parylene C was still used as a passivation layer. The internal resistance of the TEG was R_{TEG} = 281 Ω. The folded organic TEG was stored in a laboratory freezer at −8 °C for 55 h (Figure 4b), in a laboratory oven at 200 °C for 2.5 h (Figure 5c), and in a climatic chamber at 90% relative humidity for 60 h at room temperature (Figure 4d), exhibiting a relative internal resistance change ($(R\text{-}R_0)/R_0$) of only 0,2%, 0,2%, and 1,5%, respectively. No significant degradation of the internal resistance is observed over this exceptionally wide range of environmental conditions, from freezing to high temperatures and high humidity levels.

To validate the operational stability of the TEG, the *IV* characteristics were measured in its final state after all stress testing was completed. The device cumulatively underwent 55 h at −8 °C, 2.5 h at 200 °C, 60 h at 90% relative humidity, and more than four months at ambient room temperature conditions before exhibiting a $P_{max} = 0.028$ µW and a $V_{OC} = 5.8$ mV at $\Delta T = 55.7$ K (Figure S11, Supporting Information), showing a $\Phi_p = 0.771$ nW cm^{-2} K^{-2}, 6.9% more compared to the 21 thermocouples measured without the environmental stress. This finding underscores the stability of the TEG in harsh conditions.

This unmatched environmental stability makes the organic TEG highly attractive as a power source for applications like wearable electronics that must withstand sweat and varying temperatures, wireless sensors in industrial environments with extreme heat, or remote monitoring devices deployed in harsh outdoor conditions with large temperature swings and high humidity.

2.4. Comparison to the State-of-the-Art

In the comparison in Table 1, our folded organic TEG is benchmarked against other polymer-based organic TEGs from literature across variables such as number of thermocouples (n), device area (A_{TEG}), temperature gradient used for maximum power measurement (ΔT), maximum power output (P_{out}), maximum power density ($P_{density}$), normalized power density, normalized power output (c), viable storage temperature range (T), and shelf-life duration (t). The consolidated data reveals that the folded PEDOT:PSS/PBFDO device not only demonstrates a record-high normalized power output among polymer-based TEGs, but also boasts an exceptionally small footprint and unmatched stability while exploiting scalable fabrication techniques. Whereas single-metric comparisons can be misleading, this multi-variable analysis highlights the true standout attributes of the reported TEG, particularly its high performance coupled with excellent scalability and robust environmental resilience all of which are essential for real-world applications.

3. Conclusion

In this work, a scalable and fully printed, folded organic TEG is presented. First, a DMSO-based PBFDO n-type polymer ink is demonstrated to be processable through scalable printing

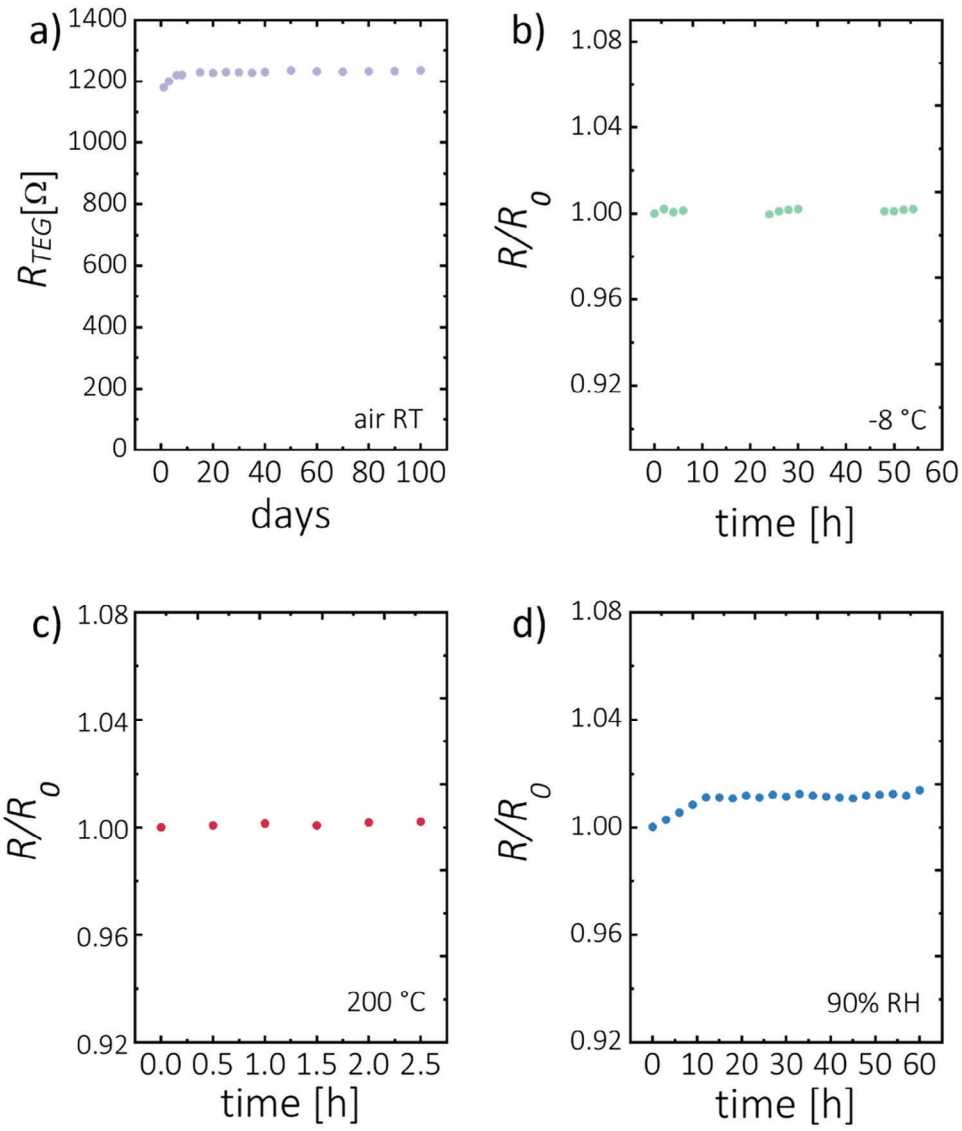

Figure 5. a) Internal resistance of the folded TEG demonstrating environmental stability when stored at room temperature. b) Change of internal resistance of the folded TEG when stored in a freezer at −8 °C. c) Change of internal resistance of the folded TEG when stored in an oven at 200 °C. d) Change of internal resistance of the folded TEG when stored in a climatic chamber at 90% relative humidity and room temperature.

techniques. The n-type ink is then integrated into a 21-leg origami-inspired architecture, realized by means of inkjet and screen-printing methods on an ultrathin, flexible parylene substrate to maximize power density. The fabricated TEG module achieves a record-high normalized power density of 0.718 nW cm^{-2} K^{-2} among reported polymer-based devices.

The significance of this work lies not only in the high-performance metrics but also in the unique combination of scalability and exceptional environmental resilience. Remarkably, the organic TEG exhibits no noticeable degradation over 90 d of shelf life and unprecedented stability across temperatures from −8 °C to 200 °C and up to 90% relative humidity. This unmatched tolerance to harsh environments for organics opens up new opportunities for organic TEGs as power sources in applications requiring resilience to extreme temperatures, moisture, and other environmental stresses.

Potential applications span wearable electronics that must withstand sweat and temperature fluctuations, wireless sensors in industrial conditions, and remote monitoring devices facing outdoor temperature swings and high humidity levels. The seamless integration of high performance, scalable printability, and robust environmental stability represents significant progress. It demonstrates the viability of organic TEGs in supplying power for next-generation sensor networks and Internet of Things devices operating in real-world, challenging environments that were previously inaccessible to this emerging technology.

4. Experimental Section

Preparation of the PBFDO Ink: The PBFDO was synthesized according to a procedure previously reported,[25] in order to obtain a solution with a final concentration of H-BDFO monomer was 10 mg mL^{-1}, typical value

for an inkjet printable ink. The final solution was filtered through a 45 mm Teflon filter and transferred to a dialysis sack with a number average molecular weight (M_n) cutoff of 10 kDa. Subsequently, the solution was further purified for two more weeks changing the solvent until the DMSO became colorless.

Characterization of the Ink and Printed Film: To analyze the rheological properties the ink viscosity at different shear rates was measured using a m-VROC microchannel rheometer with a 50 µm channel sensing unit. The measurement temperature was 30 °C. The density of the ink was measured, by weighing the ink with a Sartorius Analytical Lab balance with different volumes at RT.

To analyze the printability of the ink the surface tension was measured with a Krüss DSA100 drop-shape analyzer.

Fabrication of the Folded TEG: The screen-printing procedure was executed at RT utilizing a semi-automatic screen-printing machine (ROKUPRINT SD 05), employing two different screens measuring 600 × 300 mm in dimension. After printing each screen-printed layers of silver LOCTITE ECI 1010 E&C, the devices were annealed at 100 °C on a hot plate for 5 min. Each of the eight screen-printed layers of PEDOT:PSS Clevious SV4 PEDOT:PSS was annealed at 120 °C on a hot plate for 15 min.

Subsequently, the n-type thermoelements were patterned by printing the DMSO-based PBFDO ink (10 mg mL^{-1}) with a Pixdrop LP50 inkjet printer (20 layers) with the printer plate at 80 °C. After printing the last layer, the devices were annealed for 20 min at 90 °C on a hotplate.

Lastly, as a substrate and to electrically insulate the devices, a thin layer of parylene was deposited using the commercially available SCS PDS 2010 Labcoter 3.

Characterization of the Printed Films and the Folded TEG: The R_s of the inkjet printed DMSO-based PBFDO ink was measured with a 2612B Keithley SourceMeter, while the profile thickness was determined with a Dektak profilometer.

The temperature-dependent σ, S, and k were measured with the LINSEIS TFA instrument.

The current–voltage curves of the TEG were evaluated using an in-house measurement setup that involved two temperature-controlled Copper blocks, one serving as a heat source and the other as a heat sink. The temperature of a copper heat source and heat sink can be varied between 273 and 363 K with an accuracy of 0.1 K. A detailed analysis of the instrument and measurement errors can be found in the Supporting Information in the reference.[29]

Simulation of the Folded TEG: A simulation model COMSOL Multiphysics (version 6.2) was implemented. Three p–n thermocouples (two folded stripes) were modeled, taking into account the repetition of the device (14 folded stripes). The *Pout* evaluated was obtained forcing as heat transfer boundary conditions, three different hot side temperature T_h = 354.19 K, T_H = 345.72 K, and T_H = 336.93 K, while the cold side temperature was forced to T_c = 293 K. A detailed analysis of the simulation can be found in the reference.[33]

Harsh Environment Testing of the TEG: The resistance was measured with a UT15B Digital Multimeter. The humidity test has been done inside a Binder GmbH MKF 115 climatic chamber at RM in a dark environment. The high temperature test was made with the folded TEG inside of a Memmert VO500 PMP500 oven (without vacuum), whereas during the cold temperature test the TEG was inside of a Liebherr Comfort Fridge.

Supporting Information

Supporting Information is available from the Wiley Online Library or from the author.

Acknowledgements

I.B. and N.J.P. contributed equally to this work. This project was received funding from the research and innovation program under the Marie Skłodowska-Curie grant agreement No 955837 -HORATES. The authors acknowledge funding by the European Research Council, grant 101097876 – ORTHOGONAL. The authors also acknowledge the funding from the Deutsche Forschungsgemeinschaft (DFG, German Research Foundation) via the Excellence Cluster "3D Matter Made to Order" (EXC-2082/1-390761711). G.H.S. thanks DFG (Heisenbergprofessur, HE 7056/7-1) for the financial support. O.K. thanks the Carl Zeiss Foundation for the financial support.

Conflict of Interest

The authors declare no conflict of interest.

Data Availability Statement

The data that support the findings of this study are available from the corresponding author upon reasonable request.

Keywords

doping, energy-harvesting, organic thermoelectrics, printed electronics, thermoelectric generators

Received: June 18, 2024
Revised: August 26, 2024
Published online:

[1] M. Haras, T. Skotnicki, *Nano Energy* **2018**, *54*, 461.
[2] D. Beretta, A. Perego, G. Lanzani, M. Caironi, *Sustainable Energy Fuels* **2017**, *1*, 174.
[3] E. W. Zaia, M. P. Gordon, P. Yuan, J. J. Urban, *Adv. Electron. Mater.* **2019**, *5*, 1800823.
[4] M. Campoy-Quiles, *Philos. Trans. R. Soc. A* **2019**, *377*, 20180352.
[5] L. Huang, J. Chen, Z. Yu, D. Tang, *Anal. Chem.* **2020**, *92*, 2809.
[6] G. Chen, X. Xiao, X. Zhao, T. Tat, M. Bick, J. Chen, *Chem. Rev.* **2022**, *122*, 3259.
[7] a) B. W. Boudouris, S. K. Yee, J. Appl, M. Orrill, S. LeBlanc, M. P. Gordon, E. W. Zaia, P. Zhou, B. Russ, N. E. Coates, A. Sahu, J. J. Urban, M. Culebras, M. M. de Lima Jr, C. Gómez, A. Cantarero, A. K. Menon, E. Uzunlar, R. M. W Wolfe, J. R. Reynolds, S. R. Marder, *J. Appl. Polym. Sci.* **2017**, *134*, 44256. b) H. Fang, B. C. Popere, E. M. Thomas, C.-K. Mai, W. B. Chang, G. C. Bazan, M. L. Chabinyc, R. A. Segalman, O. Meek, A. J. Eng, *J. Appl. Polym. Sci.* **2017**, *134*, 44208.
[8] N. J. Pataki, N. Zahabi, Q. Li, P. Rossi, M. Cassinelli, M. Butti, M. Massetti, S. Fabiano, I. Zozoulenko, M. Caironi, *Adv. Funct. Mater.* **2024**, *34*, 2400982.
[9] Y. Zhang, Y. Zhu, S. Zheng, L. Zhang, X. Shi, J. He, X. Chou, Z. S. Wu, *J. Energy Chem.* **2021**, *63*, 498.
[10] L. Qi, L. Kong, Y. Wang, J. Song, A. Azam, Z. Zhang, J. Yan, *Adv. Energy Mater.* **2023**, *13*, 2302699.
[11] S. Wang, H. Sun, T. Erdmann, G. Wang, D. Fazzi, U. Lappan, Y. Puttisong, Z. Chen, M. Berggren, X. Crispin, A. Kiriy, B. Voit, T. J. Marks, S. Fabiano, A. Facchetti, S. Wang, H. Sun, M. Berggren, X. Crispin, S. Fabiano, T. Erdmann, A. Kiriy, B. Voit, U. Lappan, A. Kiriy, Z. Chen, A. Facchetti, G. Wang, T. J. Marks, D. Fazzi, et al., *Adv. Mater.* **2018**, *30*, 1801898.
[12] Y. Lu, Z. Di Yu, R. Z. Zhang, Z. F. Yao, H. Y. You, L. Jiang, H. I. Un, B. W. Dong, M. Xiong, J. Y. Wang, J. Pei, *Angew. Chem., Int. Ed.* **2019**, *58*, 11390.
[13] D. R. Hinojosa, N. J. Pataki, P. Rossi, A. Erhardt, S. Guchait, F. Pallini, C. McNeill, C. Müller, M. Caironi, M. Sommer, *ACS Appl. Polym. Mater.* **2023**, *6*, 465.

[14] Z. Di Yu, Y. Lu, Z. Y. Wang, H. I. Un, S. J. Zelewski, Y. Cui, H. Y. You, Y. Liu, K. F. Xie, Z. F. Yao, Y. C. He, J. Y. Wang, W. B. Hu, H. Sirringhaus, J. Pei, *Sci. Adv.* **2023**, *9*, eadf3495.
[15] J. Liu, B. van der Zee, R. Alessandri, S. Sami, J. Dong, M. I. Nugraha, A. J. Barker, S. Rousseva, L. Qiu, X. Qiu, N. Klasen, R. C. Chiechi, D. Baran, M. Caironi, T. D. Anthopoulos, G. Portale, R. W. A. Havenith, S. J. Marrink, J. C. Hummelen, L. J. A. Koster, *Nat. Commun.* **2020**, *11*, 5694.
[16] A. C. Hinckley, S. C. Andrews, M. T. Dunham, A. Sood, M. T. Barako, S. Schneider, M. F. Toney, K. E. Goodson, Z. Bao, A. C. Hinckley, S. C. Andrews, S. Schneider, Z. Bao, M. T. Dunham, M. T. Barako, K. E. Goodson, A. Sood, M. F. Toney, *Adv. Electron. Mater.* **2021**, *7*, 2001190.
[17] S. N. Patel, A. M. Glaudell, D. Kiefer, M. L. Chabinyc, *ACS Macro Lett.* **2016**, *5*, 268.
[18] M. Craighero, J. Guo, S. Zokaei, S. Griggs, J. Tian, J. Asatryan, J. Kimpel, R. Kroon, K. Xu, J. S. Reparaz, J. Martín, I. McCulloch, M. Campoy-Quiles, C. Müller, *ACS Appl. Electron. Mater.* **2024**, *6*, 2909.
[19] I. Brunetti, A. Dash, D. Scheunemann, M. Kemerink, *J. Mater. Res.* **2024**, *39*, 1197.
[20] Q. Li, J.-D. Huang, T. Liu, T. P. A. van der Pol, Q. Zhang, S. Y. Jeong, M.-A. Stoeckel, H.-Y. Wu, S. Zhang, X. Liu, H. Y. Woo, M. Fahlman, C.-Y. Yang, S. Fabiano, *J. Am. Chem. Soc.* **2024**, *146*, 15860.
[21] D. Yuan, W. Liu, X. Zhu, *Chem. Soc. Rev.* **2023**, *52*, 3842.
[22] I. Brunetti, F. Ferrari, N. J. Pataki, S. Abdolhosseinzadeh, J. Heier, L. Jan, A. Koster, U. Lemmer, M. Kemerink, M. Caironi, *Adv. Mater. Technol.* **2024**, *9*, 2302058.
[23] Z.-D. Yu, Y. Lu, Z.-Y. Wang, H.-I. Un, S. J. Zelewski, Y. Cui, H.-Y. You, Y. Liu, K.-F. Xie, Z.-F. Yao, Y.-C. He, J.-Y. Wang, W.-B. Hu, H. Sirringhaus, J. Pei, *Sci. Adv.* **2023**, *9*, 3495.
[24] M. Massetti, S. Bonfadini, D. Nava, M. Butti, L. Criante, G. Lanzani, L. Qiu, J. C. Hummelen, J. Liu, L. J. A. Koster, M. Caironi, *Nano Energy* **2020**, *75*, 104983.
[25] H. Tang, Y. Liang, C. Liu, Z. Hu, Y. Deng, H. Guo, Z. Yu, A. Song, H. Zhao, D. Zhao, Y. Zhang, X. Guo, J. Pei, Y. Ma, Y. Cao, F. Huang, *Nature* **2022**, *611*, 271.
[26] Z. Ke, A. Abtahi, J. Hwang, K. Chen, J. Chaudhary, I. Song, K. Perera, L. You, K. N. Baustert, K. R. Graham, J. Mei, *J. Am. Chem. Soc.* **2023**, *145*, 3706.
[27] M. Craighero, Q. Li, Z. Zeng, C. Choi, Y. Kim, H. Yoon, T. Liu, P. Sowinski, S. Haraguchi, B. Hwang, B. Mihiretie, S. Fabiano, C. Müller, *Adv. Sci.* **2024**, 2406770.
[28] I. Petsagkourakis, S. Riera-Galindo, T. P. Ruoko, X. Strakosas, E. Pavlopoulou, X. Liu, S. Braun, R. Kroon, N. Kim, S. Lienemann, V. Gueskine, G. Hadziioannou, M. Berggren, M. Fahlman, S. Fabiano, K. Tybrandt, X. Crispin, *Adv. Sci.* **2023**, *10*, 2206954.
[29] N. Pataki, P. Rossi, M. Caironi, *Appl. Phys. Lett.* **2022**, *121*, 230501.
[30] J. Hwang, Q. Zhao, M. Ahmed, A. C. Yakisan, M. F. Espenship, J. Laskin, B. M. Savoie, J. Mei, *Angew. Chem., Int. Ed.* **2024**, *63*, 202401465.
[31] D. Scheunemann, E. Järsvall, J. Liu, D. Beretta, S. Fabiano, M. Caironi, M. Kemerink, C. Müller, *Chem. Phys. Rev.* **2022**, *3*, 021309.
[32] A. G. Rösch, A. Gall, S. Aslan, M. Hecht, L. Franke, M. M. Mallick, L. Penth, D. Bahro, D. Friderich, U. Lemmer, *npj Flexible Electron.* **2021**, *5*, 1.
[33] L. Franke, A. G. Rösch, Q. Zhang, M. I. Khan, Z. Long, I. Brunetti, M. N. Joglar, A. M. Lara, C. D. Simão, H. Geßwein, Y. M. Eggeler, U. Lemmer, M. M. Mallick, *Adv. Funct. Mater* **2024**, 2403646.
[34] Y. Liu, D. R. Villalva, A. Sharma, M. A. Haque, D. Baran, *ACS Appl. Mater. Interfaces* **2021**, *13*, 411.
[35] O. Zapata-Arteaga, B. Dörling, A. Perevedentsev, J. Martín, J. S. Reparaz, M. Campoy-Quiles, *Macromolecules* **2020**, *53*, 609.
[36] D. R. Villalva, M. A. Haque, M. I. Nugraha, D. Baran, *ACS Appl. Energy Mater.* **2020**, *3*, 9126.
[37] C. Zheng, L. Xiang, W. Jin, H. Shen, W. Zhao, F. Zhang, C. Di, D. Zhu, C. Z. Zheng, L. Y. Xiang, W. L. Jin, H. G. Shen, W. R. Zhao, C. Di, D. B. Zhu, F. J. Zhang, *Adv. Mater. Technol.* **2019**, *4*, 1900247.
[38] P. Aranguren, A. Roch, L. Stepien, M. Abt, M. Von Lukowicz, I. Dani, D. Astrain, *Appl. Therm. Eng.* **2016**, *102*, 402.
[39] A. Lund, Y. Tian, S. Darabi, C. Müller, *J. Power Sources* **2020**, *480*, 228836.
[40] D. Kim, D. Ju, K. Cho, *Adv. Mater. Technol.* **2018**, *3*, 1700335.
[41] C. Y. Yang, Y. F. Ding, D. Huang, J. Wang, Z. F. Yao, C. X. Huang, Y. Lu, H. I. Un, F. D. Zhuang, J. H. Dou, C. an Di, D. Zhu, J. Y. Wang, T. Lei, J. Pei, *Nat. Commun.* **2020**, *11*, 3292.